This is a non-peer reviewed preprint submitted to EarthArXiv, under review at *Geophys. J. Int.*

The Stability of Frictional Sliding on Dip-Slip and Finite-Length Faults

Rob M. Skarbek*[1]

[1]Planetary Science Institute

1 Abstract

This paper examines the linear stability of sliding on faults embedded in a 2D elastic medium that obey rate and state friction and have a finite length and/or are near a traction-free surface. Previous work typically has examined either spring-slider systems or infinitely long faults. Results are obtained using a numerical technique that allows for analysis of systems with geometrical complexity, and/or heterogeneous material properties; however only systems with homogeneous frictional and material properties are examined. Some analytical results are also obtained. On velocity-weakening faults with finite length, there is a critical fault length L^* for unstable sliding that is analogous to the critical nucleation length h^* that is usually derived from spring-slider or infinite fault systems. Faults longer than L^* are unstable to perturbations of any size. On vertical strike-slip faults $L^* = h^*/e$. For dip-slip faults near a traction-free surface, $L^* \leq h^*/e$ and is a function of dip angle β, burial depth d, and friction coefficient. In particular, L^* is at least an order of magnitude smaller than h^* on shallowly dipping ($\beta < 10°$) faults that intersect the traction-free surface. Additionally, $L^* = h^*/e$ on dip-slip faults with burial depths $d \geq h^*$. For sliding systems that can be treated as a thin layer, such as landslides, glaciers, or ice streams, $L^* = h^*/2$. Finally, conditions are established for unstable sliding on infinitely-long, velocity-strengthening faults that are parallel to a traction-free surface.

2 Introduction

How does the geometry of fault systems affect the stability of frictional sliding? Most knowledge of frictional stability comes from analyses of spring-slider systems, or systems consisting of an infinitely long fault in an infinite elastic medium (e.g. *Ruina*, 1983; *Rice and Ruina*, 1983; *Rice et al.*, 2001). These two systems do not include important aspects of fault geometry such as proximity to a traction-free surface, fault dip angle, or finite fault length. This paper examines the sliding stability of finite-length faults that obey rate and state friction (RSF) and are embedded in a 2D elastic continuum with homogeneous material properties.

The specific finite-length geometries considered are: faults in an infinite full-space; faults parallel to a traction-free surface; and dip-slip faults and vertical strike-slip faults in a half-space. Including these features provides more accurate assessments of sliding stability of natural fault systems. First, because all faults have a finite length and second, because many faults are near the surface of the earth or the seafloor. Additionally, landslides, ice streams, and glaciers also exhibit sliding behavior

---

*rskarbek@psi.edu

that can be described by frictional processes. The results show that these basic geometrical effects cause significant departures from long-standing results on stability behavior.

For a fault in an elastic medium, the stability of sliding can be assessed by considering a balance between the rate at which elastic stress stored in the fault system can be unloaded, and the rate at which shear stress on the fault is reduced (i.e. fault weakening) in response to sliding (e.g. *Scholz*, 2019). Unstable sliding (in the form of an earthquake or slow slip event) initiates when the fault weakening rate is higher than the elastic unloading rate. For frictional sliding, the changes in shear stress on a fault are described by the RSF equations; wherein the evolution of the friction coefficient μ on a surface is a function of the sliding rate v and an internal state variable θ

$$\mu = \mu_0 + a \ln\left(\frac{v}{v_0}\right) + b \ln\left(\frac{v_0 \theta}{d_c}\right), \tag{1}$$

where a, b, and d_c are material dependent frictional parameters, and μ_0 is a reference coefficient such that $\mu = \mu_0$ for steady sliding at v_0 (*Dieterich*, 1979; *Ruina*, 1983; *Marone*, 1998). The evolution of the state variable is commonly described using the aging or slip laws:

$$\text{aging law:} \quad \frac{\partial \theta}{\partial t} = 1 - \frac{v\theta}{d_c}, \quad \text{slip law:} \quad \frac{\partial \theta}{\partial t} = -\frac{v\theta}{d_c} \ln\left(\frac{v\theta}{d_c}\right). \tag{2}$$

For velocity-weakening friction ($a - b < 0$; or $a/b < 1$), fault weakening will occur due to a reduction in the friction coefficient as sliding rate increases. Weakening can also occur due to a coupling between fault slip and changes in normal stress, which can lead to unstable behavior for velocity-strengthening friction below some critical value of a/b. This effect has been shown to exist on bimaterial and poroelastic faults (*Rice et al.*, 2001; *Heimisson et al.*, 2019), and on faults that lack geometric reflection symmetry across the sliding surface (*Aldam et al.*, 2016). In fact, lack of geometric reflection symmetry is a very general feature of fault systems. So too then is the possibility of unstable behavior on velocity-strengthening faults. The results in this paper take a first step in establishing the range of parameters where this behavior occurs on faults that are near a traction-free surface.

Linear stability analysis of faults in an elastic continuum leads to the concept of a nucleation length h^* (*Ruina*, 1983; *Rice and Ruina*, 1983). The nucleation length is usually interpreted as the minimum length of a failing fault patch that is required for an unstable sliding event to develop (e.g. *Dieterich*, 1992; *Scholz*, 2019). In this interpretation, failure on velocity-weakening fault patches with lengths smaller than h^* cannot develop into an unstable event. The value of h^* is usually derived using one of two different methods.

First, h^* can be found analytically for the special case of an *infinitely long* fault with constant frictional properties and effective normal stress σ, embedded in an infinite, 2D elastic full-space with homogeneous properties. Allowing the fault to be infinitely long simplifies the mathematical analysis sufficiently to obtain an equation for h^*:

$$h^*_F = \frac{\pi G' d_c}{\sigma(b - a)}, \tag{3}$$

where G' is the effective shear modulus (*Rice and Ruina*, 1983; *Rice et al.*, 2001). Here the symbol h^*_F is used to denote the special value of the nucleation length for a homogeneous fault in a full-space. Because the derivation of h^*_F involves an infinitely long fault, its proper technical definition is the critical wavelength of an infinitely long perturbation to the slip velocity; perturbations with wavelengths smaller than h^*_F will not develop into unstable events (*Rice and Ruina*, 1983; *Rice et al.*, 2001). Therefore in this analysis, h^*_F does not represent a minimum contact or patch length.

Equation (3) without the factor of π can also be obtained by equating the critical stiffness of an RSF spring-slider system to the stiffness of a crack subjected to anti-plane strain conditions and a constant stress drop; other numerical prefactors are obtained depending on the assumed stress and strain conditions (see Table 1 in *Dieterich*, 1992). Assuming a single value of stiffness for a fault simplifies the mathematics and allows an equation for h^*_F to be obtained. However, faults do not possess a material property called "stiffness" in the same sense that they possess frictional or elastic properties. Instead, the stiffness of a fault is a quantity that evolves through space and time as the fault slips (e.g. *Horowitz and Ruina*, 1989).

Natural faults are neither infinitely long, nor do they posses an easily defined stiffness. While these assumptions lead to the simple and highly useful definition of h^*_F, they are not representative of natural conditions. In this paper, these difficulties are overcome by using a numerical method for conducting linear stability analysis of 2D finite-length fault systems. The method can be applied to any fault system for which stress change functions are available (defined in the next section), and can accommodate features such as heterogeneous material properties or multiple faults. Analytical results are also obtained for a special case.

The results of this paper show that for finite-length faults, once the fault length is larger than some critical value L^*, a perturbation of any size will nucleate an unstable sliding event. Throughout this paper values of h^* are referred to as "critical wavelengths" and the symbol L^* is used to denote a "critical fault length". For both h^* and L^*, subscripts are used to differentiate between specific geometries. On vertical strike-slip faults $L^* = h^*_F/e$. For dip-slip faults near a traction-free surface, $L^* \leq h^*_F/e$ and is a function of dip angle β, burial depth, and friction coefficient. However, $L^* = h^*_F/e$ for dip-slip faults where the up-dip edge is buried at a depth $\geq h^*_F$. The results also establish conditions for linear instability under velocity-strengthening friction on infinitely long faults that are parallel to a traction-free surface.

3 Methods

Consider a fault of length L that obeys equation (1) and either of equations (2), and denote the position along the fault by ξ. Assume also that the fault is embedded in a 2D homogeneous elastic medium with shear modulus G and Poisson ratio ν; and define an effective shear modulus G' such that $G' = G$ for anti-plane sliding, and $G' = G/(1-\nu)$ for in-plane sliding. A linear stability analysis of the fault's sliding motion can be conducted according to the following steps. **(1)** Write the system of nonlinear equations governing the evolution of sliding velocity $v(\xi,t)$ and state variable $\theta(\xi,t)$ along the fault. **(2)** Determine a uniform steady state of the system such that $v(\xi,t) = v_0$ and $\theta(\xi,t) = \theta_0$. **(3)** Obtain a linearized system of equations by computing the Jacobian matrix $\boldsymbol{J}$ of the nonlinear system, and evaluating it at the uniform steady state so that $\boldsymbol{J}_0 = \boldsymbol{J}(v_0,\theta_0)$. **(4)** Determine the stability of the linear system by examining the eigenvalues of $\boldsymbol{J}_0$. If any eigenvalue has a positive real part, then the system is unstable. Depending on the complexity of the system, the eigenvalues can be determined analytically and/or numerically.

Step 1. For quasi-static sliding, the velocity of the fault is governed by a balance between frictional resistance $\tau_F = \mu\sigma$ and shear stresses resolved upon the fault $\tau = \tau_0 + \tau_E$, where τ_E is the change in shear stress due to gradients in slip along the fault, and τ_0 is the shear stress on the fault in the absence of any slip. As with the shear stress, the normal stress on the fault is $\sigma = \sigma_0 + \sigma_E$. Following previous linear stability studies, externally applied stresses are not included (e.g. *Rice and Ruina*, 1983; *Rice et al.*, 2001). The stress balance changes in time as $\dot{\mu}\sigma = \dot{\tau}_E - \mu\dot{\sigma}_E$, and by making use of equation (1), the sliding velocity of the fault can be written as

$$\dot{v}(\xi, t) = F(v, \theta) = \frac{v}{a}\left[\frac{\dot{\tau}_E - \mu\dot{\sigma}_E}{\sigma} - \frac{b\dot{\theta}}{\theta}\right] , \tag{4}$$

The evolution of the state variable can simply be written as $\dot{\theta}(\xi, t) = H(v, \theta)$, since only the aging and slip laws are considered here and both state variable laws have the same linearization (e.g. *Ruina*, 1983). The nonlinear governing equations of the system are now represented by the functions $F(v, \theta)$ and $H(v, \theta)$.

For quasi-static sliding, the changes in shear and normal stress are functions of the slip distribution $\delta(\xi, t)$, so that $\tau_E = T(\xi, \delta)$ and $\sigma_E = N(\xi, \delta)$. The functions $T(\xi, \delta)$ and $N(\xi, \delta)$ are the stress change functions mentioned in the Introduction. They must be determined based on the geometrical aspects of the fault system and in general will depend on fault position ξ. These functions also have the property that $\dot{\tau}_E = T(\xi, v)$ and $\dot{\sigma}_E = N(\xi, v)$ (e.g. *Viesca*, 2016a,b). Both $T(\xi, \delta)$ and $N(\xi, \delta)$ are equal to zero if there is no slip gradient.

Step 2. The uniform steady state of the system satisfies the conditions $F(v_0, \theta_0) = 0$ and $H(v_0, \theta_0) = 0$. Assume that the entire fault is sliding at steady-state with velocity v_0, such that $T(\xi, v_0) = N(\xi, v_0) = 0$. For both the aging and slip laws, $H(v_0, \theta_0) = 0$ when $\theta_0 = d_c/v_0$. These conditions satisfy $F(v_0, \theta_0) = 0$, so the uniform steady state of the nonlinear system is $(v_0, d_c/v_0)$.

Step 3. To linearize the equations about the uniform steady state, first define

$$\mathbf{w}(\xi, t) = \begin{bmatrix} v(\xi, t) - v_0 \\ \\ \theta(\xi, t) - \theta_0 \end{bmatrix} \tag{5}$$

where $\mathbf{w}(\xi, t)$ is a small perturbation away from (v_0, θ_0). Now the linearized equations can be written as $\dot{\mathbf{w}} = \boldsymbol{J}_0\mathbf{w}$. The Jacobian matrix $\boldsymbol{J}_0$ is most conveniently expressed in terms of the dimensionless variables: $\hat{t} = (v_0/d_c)t$, $\hat{v} = v/v_o$, and $\hat{\theta} = (v_0/d_c)\theta$, such that the uniform steady state becomes $(\hat{v}_0, \hat{\theta}_0) = (1, 1)$. Then $\boldsymbol{J}_0$ can be written as

$$\boldsymbol{J}_0 = \begin{bmatrix} \frac{\partial \hat{F}_0}{\partial \hat{v}} & \frac{\partial \hat{F}_0}{\partial \hat{\theta}} \\ \\ \frac{\partial \hat{H}_0}{\partial \hat{v}} & \frac{\partial \hat{H}_0}{\partial \hat{\theta}} \end{bmatrix} = \begin{bmatrix} \left(\frac{b}{a}\right)\left[\frac{1}{b}(\hat{T}_{\hat{v}} - \mu_0\hat{N}_{\hat{v}}) + 1\right] & \left(\frac{b}{a}\right)\boldsymbol{I} \\ \\ -\boldsymbol{I} & -\boldsymbol{I} \end{bmatrix} \tag{6}$$

where $\hat{F}_0 = \hat{F}(\hat{v}_0, \hat{\theta}_0)$, $\hat{G}_0 = \hat{G}(\hat{v}_0, \hat{\theta}_0)$, $\boldsymbol{I}$ is the identity matrix, and $\hat{T}_{\hat{v}}$ and $\hat{N}_{\hat{v}}$ denote derivatives with respect to $\hat{v}$. Some additional mathematical steps are provided in Appendix A.

Step 4. The eigenvalues and eigenvectors of $\boldsymbol{J}_0$ determine solutions to the linearized system ($\dot{\mathbf{w}} = \boldsymbol{J}_0\mathbf{w}$) of the form $\mathbf{w}(\xi, t) \propto \boldsymbol{w}(k\xi)e^{pt}$. The eigenvectors $\boldsymbol{w}(k\xi)$ represent small spatial perturbations of wavenumber k to the uniform steady state. The eigenvalues p are the corresponding growth rates of those perturbations. If all of the eigenvalues of $\boldsymbol{J}_0$ have a negative real part, then the system is linearly stable. If any eigenvalue has a positive real part then the system is linearly unstable (*Strogatz*, 2018, e.g.).

3.1 Analytical Stability Analysis

For analytical results, $\boldsymbol{J}_0$ can be treated as a 2×2 matrix. Then the eigenvalues are found by solving $\det(\boldsymbol{J}_0 - p\boldsymbol{I}) = 0$, where det() denotes the determinant of the matrix, such that

$$p^2 + \left[1 - \tfrac{b}{a}(\Gamma + 1)\right]p - \left(\tfrac{b}{a}\right)\Gamma = 0 , \quad \Gamma = \tfrac{1}{b}(\hat{T}_{\hat{v}} - \mu_0\hat{N}_{\hat{v}}) . \tag{7}$$

Depending on the complexity of the problem, equation (7) can be solved for the eigenvalues p. However, in cases where T_v and N_v are purely real functions, the eigenvalues do not need to be explicitly determined; the stability of the system can be determined from conditions on $\det(\boldsymbol{J}_0) = -(b/a)\Gamma$ and $\mathrm{Tr}(\boldsymbol{J}_0) = (b/a)(\Gamma + 1) - 1$, where Tr() denotes the trace of the matrix. The system is unstable if $\det(\boldsymbol{J}_0) > 0$ and $\mathrm{Tr}(\boldsymbol{J}_0) > 0$ (e.g. *Strogatz*, 2018, Figure 5.2.8). Since it is generally the case that $b/a > 0$, the determinant condition becomes $\Gamma < 0$. The trace instability condition can be written as

$$\left(\frac{b}{a}\right)\left[\frac{1}{b}(\hat{T}_{\hat{v}} - \mu_0 \hat{N}_{\hat{v}}) + 1\right] - 1 > 0 \; . \tag{8}$$

Equation (8) can be used to obtain analytical stability results. For example, in a spring-slider system $N_v = 0$ and $T_v = -K$, where K is the spring stiffness. Then solving equation (8) for K will yield the usual relation for the critical spring stiffness (see Appendix B.1).

For faults in a 2D medium, analytical results can be obtained by specifying the functional form of the spatial perturbation $\boldsymbol{w}(k\xi)$. For infinitely long faults there are no restrictions on the values of k because the fault has no boundaries. Then the general solution to the linear equations is

$$\mathbf{w}(\xi, t) = \int_{-\infty}^{\infty} A(k) \exp{(pt + ik\xi)} dk \; , \tag{9}$$

where $A(k)$ is determined by a Fourier transform of the initial conditions (*Pivato*, 2010). The steps of deriving equation (3) using equations (8) and (9) are detailed in Appendix B.2.

For a finite-length fault with a uniform steady state velocity v_0, the sliding velocity must remain v_0 at the boundaries, and so $\boldsymbol{w}(k\xi)$ must be equal to zero at the boundaries. If the fault is defined over $\xi = [0, L]$, the general solution to the linear equations that satisfies these boundary conditions is

$$\mathbf{w}(\xi, t) = \sum_n \boldsymbol{A}_n e^{\lambda t} \sin[n\pi\xi/L] \; , \tag{10}$$

where the constants $\boldsymbol{A}_n$ are determined by Fourier series expansion of the initial conditions (*Pivato*, 2010). The allowable wavenumbers are $k = n\pi/L$ (for $n = 1, 2, ...$), analogous to the normal modes on a vibrating string. So, for finite-length faults the possible values of k are discrete and scaled by the fault length L, and this has important consequences for the stability behavior.

3.2 Numerical Stability Analysis

For numerical results, if the fault is discretized into N_e elements of length $d\xi$, then $\boldsymbol{J}_0$ becomes a $2N_e \times 2N_e$ block matrix where in general, the upper-left block $\partial\hat{F}_0/\partial\hat{v}$ is dense and the other blocks are sparse diagonal matrices. In discrete form, the functions $T(\xi, v)$ and $N(\xi, v)$ become linear operators on the slip velocity. For example, $T(\xi, v) \to \boldsymbol{T}\boldsymbol{v}$, and $T_v \to \boldsymbol{T}$, where $\boldsymbol{T}$ is an $N_e \times N_e$ matrix and $\boldsymbol{v}$ is a vector of length N_e. The stability condition given by equation (8) is only valid for 2×2 matrices (e.g. *Luís*, 2021). For numerical analysis the eigenvalues must be explicitly calculated to search for conditions where the system is unstable (e.g. *Viesca*, 2016a,b; *Ray and Viesca*, 2017; *Viesca*, 2023). The eigenvalues can be directly computed using standard numerical routines; here the MATLAB functions *eig* and *eigs* are used.

4 Results

Results are presented first for a finite-length fault that is parallel to a traction-free surface, using a thin-layer approximation for the stress change functions. Analytical results are obtained for

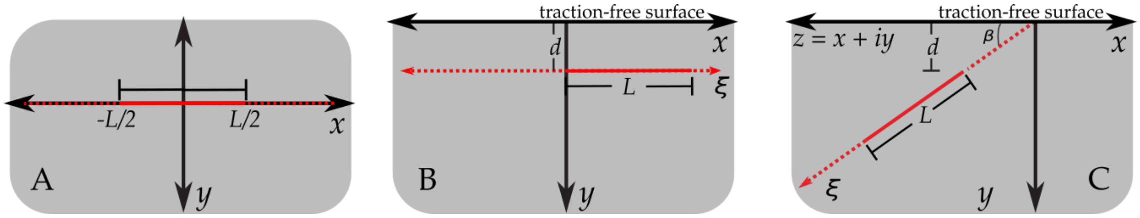

Figure 1: Diagrams of the fault system geometries used in this paper. In each panel, a fault of length L is located by the solid red line; the dashed red line is the extension along the ξ-axis. **(A)** A fault in an infinite full-space. **(B)** A fault at a depth d, parallel to a traction-free surface; both infinite and finite length systems are considered. **(C)** A fault of length L, dipping at an angle β relative to a traction-free surface, with its up-dip edge at a depth d. In panels B and C, the traction-free upper surface is defined by $y = 0$.

the thin-layer system, which provide insight into more complex systems; numerical results for this system are presented as well. Next results are obtained numerically for vertical strike-slip faults, as well as faults in an infinite full-space. Finally, dip-slip faults of any orientation in a system with a traction-free surface are examined.

4.1 Thin Layer Approximation

Consider a fault of length L that is parallel to a traction-free surface at a depth d (Figure 1B). In general, this system will have a nonzero $N(\xi, v)$ for in-plane sliding (see Section 4.3). However, when $d \ll L_b = d_c G'/(b\sigma_0)$ then $N(\xi, v) = 0$ and the change in shear stress is (*Viesca*, 2016a)

$$T(\xi, v) = (dE')\frac{\partial^2 v}{\partial \xi^2}\ , \quad E' = \begin{cases} \frac{2G}{1-\nu}, & \text{anti-plane sliding} \\ G, & \text{in-plane sliding} \end{cases} \tag{11}$$

For an infinitely long fault in this system, the critical wavelength is (*Viesca*, 2016b)

$$h^*_L = \frac{2\pi L_{bh}}{(1 - a/b)^{1/2}}\ , \tag{12}$$

where $L_{bh} = \sqrt{dE'd_c/(b\sigma_0)}$ (see Appendix B.3).

Due to the simplicity of equation (11), analytical results can be obtained for finite length faults in this system. By assuming a solution for $v(\xi, t)$ of the form of equation (10), the normalized shear stress change function becomes $\hat{T}_v/b = -(n\pi L_{\text{bh}}/L)^2$. Then the instability condition for the fault length, via equation (8), becomes

$$L > \frac{n\pi L_{\text{bh}}}{(1 - a/b)^{1/2}} = \frac{nh^*_L}{2}\ . \tag{13}$$

Since the right hand side of equation (13) is smallest at $n = 1$, the critical fault length is

$$L^*_L = \frac{h^*_L}{2}\ . \tag{14}$$

Equation (14) indicates that the fault becomes unstable when it is long enough that the wavelength λ of the first mode ($n = 1$) of equation (10) becomes equal to $\lambda = 2\pi/k = 2L = h^*_L$.

Numerical stability analysis for this system can be conducted after discretizing equation (11). The stability boundary can be numerically determined by choosing a value of a/b, then computing

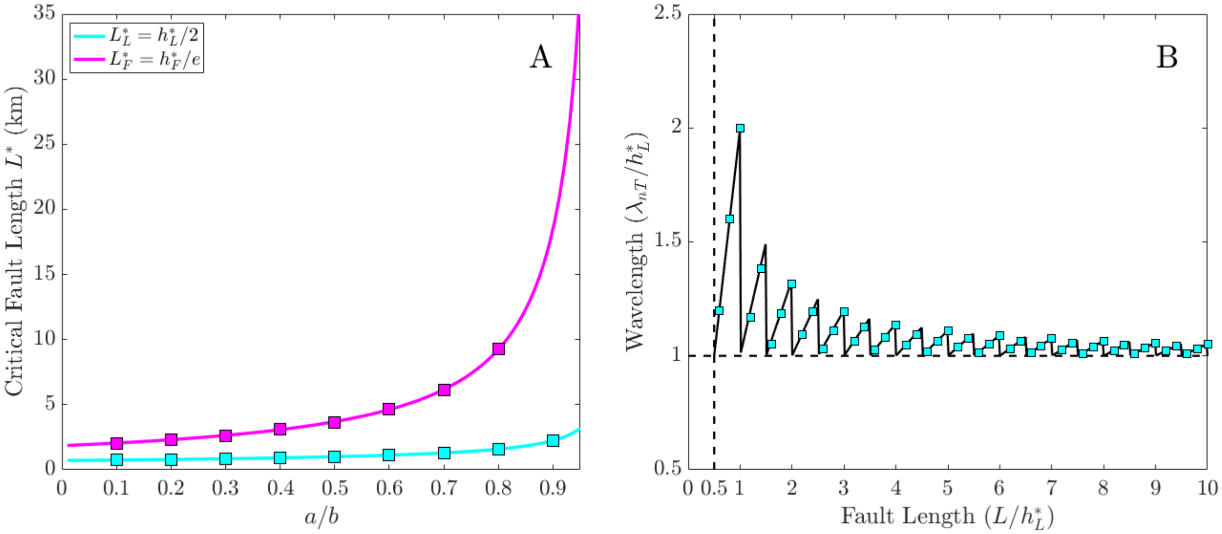

Figure 2: **(A)** Examples of critical faults lengths L^* for the thin layer (cyan) and strike-slip/full-space (magenta) systems. Solid lines correspond to expressions as shown in the legend; squares are numerically determined boundaries. **(B)** Wavelength of the highest unstable mode number as a function of the fault length for the thin layer system. Both wavelengths and fault lengths are normalized by the critical wavelength h_L^*. The black line shows the analytical result given by equation (15), the cyan squares show the numerically determined wavelengths. For all calculations $L_b = 1600$ km; for thin layer calculations $d = 0.01L_b$. Grid spacing for numerical calculations: $d\xi = L_b/20$ for full-space and $d\xi = L_{bh}/20$ for thin layer.

the stability of the system for different values of L. Then the critical fault length coincides with the value of L where the stability changes. Figure 2A displays the results of this process for nine different values of a/b, and shows that the numerically determined boundary confirms the result of equation (14).

As the fault length increases above L_L^*, progressively higher mode numbers will become unstable and the wavelength of the highest unstable mode number will approach h_L^* as $L \to \infty$. From equation (13), the total number of unstable modes that a fault can host is $n_T = \mathrm{Fl}(2L/h_L^*)$, where $\mathrm{Fl}(q)$ gives the greatest integer less than or equal to some quantity q. The wavelength of the highest mode number n_T is

$$\lambda_{n_T} = \frac{2L}{\mathrm{Fl}(2L/h_L^*)} \ , \quad \text{and} \quad \lim_{L\to\infty} \lambda_{n_T} = h_L^* \ . \tag{15}$$

Equation (15) predicts that $\lambda_{n_T} \geq h_L^*$ and approaches h_L^* with a type of saw-tooth pattern as $L \to \infty$ (Figure 2B). This result can also be confirmed numerically by computing the wavelength of the eigenvector for the highest unstable mode as a function of the fault length for $L > L_L^*$ (Figure 2B). The close agreement between the analytical and numerical analyses both validates the numerical method and confirms the behavior for finite length faults.

Another important consequence of finite fault length is that for faults longer than L_L^*, there is no minimum failure patch length required to generate an unstable sliding event. Since equation (10) is a superposition of all mode numbers, instability will occur if any mode has a positive growth rate p. Thus, any set of initial conditions that gives $A_n \neq 0$ for an unstable mode will generate an instability; and there are no conditions on the length scale of the perturbation. This is illustrated further in the next section.

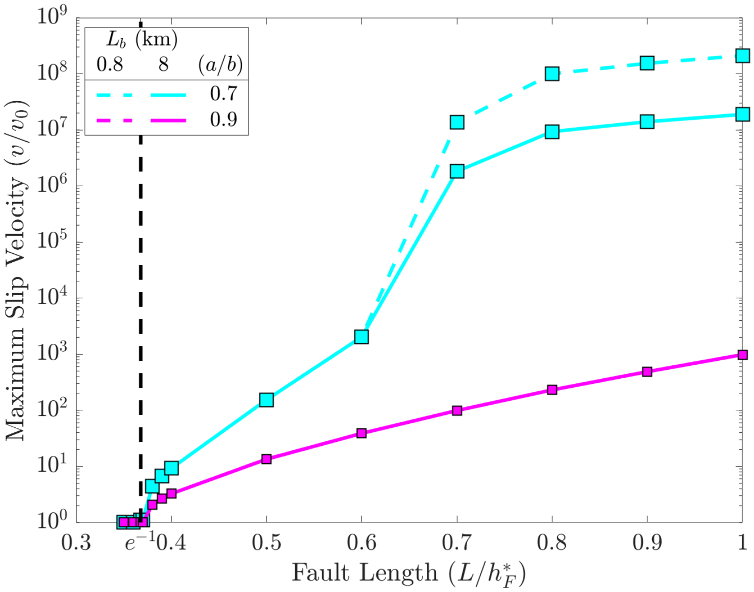

Figure 3: Normalized maximum slip velocities as a function of normalized fault length for faults in a full-space, or vertical strike-slip faults in a half-space. Each square corresponds to an individual simulation. Colors correspond to values of (a/b) and line styles to values of L_b, as indicated in the legend. Note, the solid and dashed lines for $(a/b) = 0.9$ overlap each other. The stability boundary $L/h_F^* = e^{-1}$ is indicated by the vertical black, dashed line. Grid spacing for simulations: $d\xi = L_b/20$.

4.2 Vertical Strike-Slip Faults in a Half-Space and Full-Space Faults

Now consider a fault of length L embedded in a homogeneous full-space (Figure 1A). For this system $N(\xi, v) = 0$ and the change in shear stress is given by (e.g. *Segall*, 2010)

$$T(\xi, v) = \frac{G'}{2\pi} \int_{-L/2}^{L/2} \frac{\partial v/\partial s}{s - \xi} ds \ . \tag{16}$$

This stress change function is also valid for a vertical strike-slip fault in a half-space, in which case the integration is taken over $[d, d + L]$ and $G' = G$ (Figure 1C with $\beta = 90°$). For an infinitely long fault, $L \to \infty$, and equation (16) takes the form of a Hilbert transform. Then the nucleation wavelength h_F^* given by equation (3) can be obtained from equation (8); see Appendix B.2.

For a finite-length fault, the bounds of the integral in equation (16) prevent analytical analysis. Instead, the stability analysis can be conducted numerically in the same manner as for the thin layer system. The critical fault length for the full-space system coincides with $L_F^* = h_F^*/e$ (Figure 2A).

This boundary is also confirmed by simulations of the full governing equations using equation (16). Figure 3 shows the results of four sets of simulations using two values of a/b and L_b. In these simulations the initial conditions are set to the uniform steady state values, except for one node at the center of the fault where $v(\xi = 0, t = 0) = 0.99v_0$. Hence the spatial extent of the initial perturbation is as small as the numerical discretization allows.

For each pair of $(a/b,\ L_b)$ values, the simulations were run with different fault lengths until a consistent cycle of sliding events developed, or the sliding velocity reached a uniform steady state such that $v(\xi, t) = v_0$. The stability boundary coincides with the fault length that separates growth

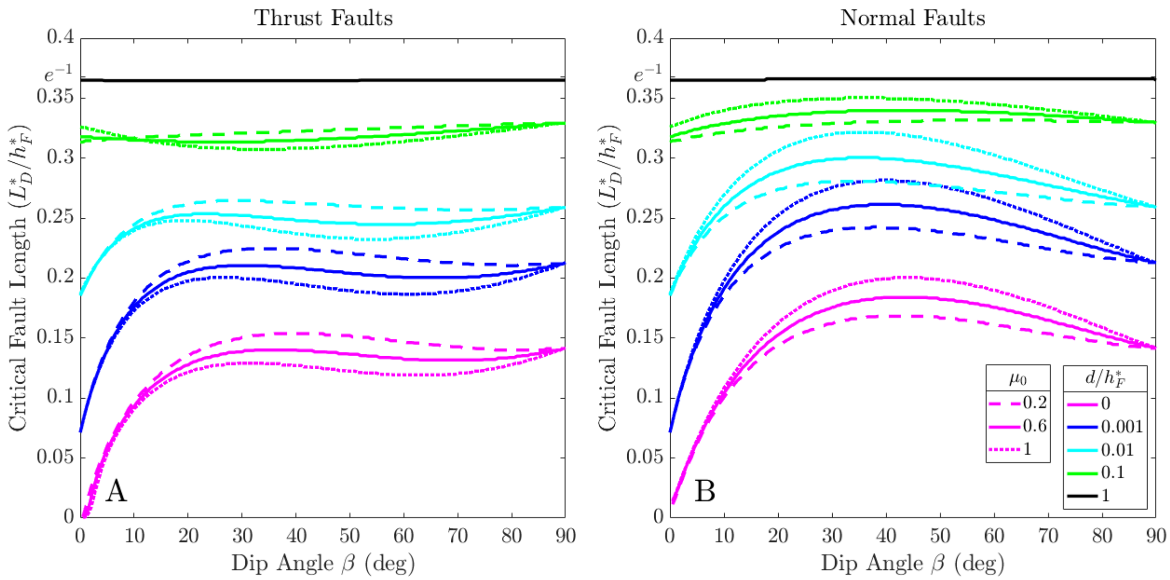

Figure 4: Critical fault lengths L_D^* for thrust and normal faults as a function of dip angle β, burial depth d, and friction coefficient μ_0. Critical fault lengths and burial depths are normalized by h_F^*. For both panels, values of d are indicated by colors, and values of μ_0 by line styles as indicated in the legend. The solid black lines are equal to e^{-1} to within 0.8%.

and decay of the initial perturbation, as indicated by the maximum slip velocity. In all four of the cases, this boundary coincides with $L = h_F^*/e$. As for the thin layer system, these results confirm the effects of finite fault length and also the lack of a minimum perturbation length scale.

4.3 Dip-Slip Faults

For the final system examined here, consider in-plane sliding on a fault that is dipping at an angle β relative to the traction-free surface of a homogeneous, elastic half-space (Figure 1C). The up-dip edge of the fault is buried at a depth d below the traction-free surface. Both the full-space and parallel fault geometries are special cases of this dipping fault geometry. The full-space geometry is obtained when $d \to \infty$, and the parallel fault geometry is obtained when $d \neq 0$ and $\beta = 0$.

Stress change functions for the half-space geometry are available in the literature (*Dmowska and Kostrov*, 1973; *Freund and Barnett*, 1976; *Rudnicki and Wu*, 1995), and can be written as

$$T(\xi, v) = \int_{l}^{l+L} \Psi(z, \beta) \frac{\partial v}{\partial s} ds \ , \tag{17}$$

where $l = d/\sin(\beta)$, and $\Psi(z, \beta)$ is an analytic function of the complex variable $z = x + iy$ (*England*, 2003). A similar expression holds for $N(\xi, v)$. A derivation of these functions is presented in Appendix C. Note that these stress change functions are equivalent to using the *Okada* (1992) solutions for the middle of a very long dip-slip fault (e.g. *Liu and Rice*, 2007).

4.3.1 Velocity-Weakening Behavior

Critical fault lengths L_D^* for the dipping geometry can be determined by choosing a burial depth d and dip angle β, then checking the stability of the system for different values of L. For fixed values of d and β, changing the value of L corresponds to changing the down-dip depth of the fault. This

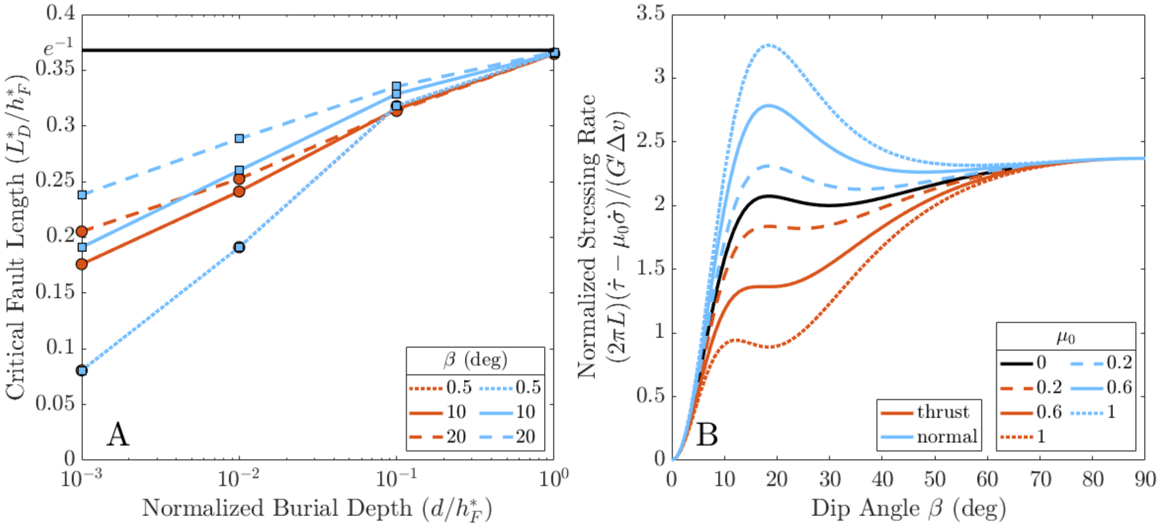

Figure 5: **(A)** Examples of critical fault lengths for thrust and normal faults as a function of dip angle for $\beta = 0.5°$, $10°$, $20°$. **(B)** Normalized stressing rates $(2\pi L)(\dot{\tau}_E - \mu\dot{\sigma}_E)/(G'\Delta v)$ for thrust and normal faults. For both panels the sense of slip is indicated by colors as shown in the legend in panel B.

calculation was repeated for dip angles in the range $\beta = 0° - 90°$ and burial depth values $d/h_F^* = 0$, 10^{-3}, 10^{-2}, 10^{-1}, 1; for $\beta = 0°$, $d = 0$ was omitted. This process was carried out for values of $\mu_0 = 0.2$, 0.6, 1, for both thrust and normal faults (Figure 4). At depths $d > h_F^*$, the results are identical to $d = h_F^*$; so Figure 4 shows critical fault lengths for both thrust and normal faults in any possible orientation. Values of L_D^* depend primarily on the dip angle and the burial depth, up to $d = h_F^*$ where the stability behavior becomes identical to that of a fault in a full-space. For burial depths $d < h_F^*$, the critical fault length is approximately a log-linear function of d (Figure 5A).

There is a somewhat complex dependence of L_D^* on the dip angle that is different for thrust and normal faults. There is also a secondary dependence on the value of μ_0 that depends on the sense of slip. For both thrust and normal faults, L_D^* increases with dip angle up to a value of 20° – 40°, depending on the burial depth and sense of slip. For thrust faults, L_D^* then decreases to a secondary minimum before increasing again as $\beta \to 90°$. For normal faults, L_D^* reaches a maximum value then decreases as $\beta \to 90°$. Increasing the value of μ_0 decreases L_D^* for thrust faults, and does the opposite for normal faults. Values of L_D^* can become quite small on shallowly dipping faults that are near to the traction-free surface. In particular, as $\beta \to 0°$ on faults that break the surface ($d = 0$), $L_D^*/h_F^* \to 10^{-2}$ on normal faults, and appears to approach zero on thrust faults.

The dependence of L_D^* on β and μ_0 can mostly be explained by considering the on-fault stressing rates due to a uniform slip velocity distribution Δv on a dipping fault of length L with burial depth $d = 0$. The elastic stressing rate on the fault is $\dot{\tau}_E - \mu\dot{\sigma}_E$ (see Section 3, Step 1), which can be computed by evaluating the stress change functions at the center of the fault $\xi = L/2$ (e.g. *Kato and Hirasawa*, 1997). The stressing rate has a dependence on β and μ_0 that shares some of the same features as that of L_D^*; including similar behavior as $\beta \to 0°$ and $\beta \to 90°$, and the same style of dependence on μ_0 for thrust and normal faults (Figure 5B).

The stressing rate calculation also provides an explanation for why values of L_D^* become very small at shallow dip angles. Sliding instability develops when the frictional weakening rate $\dot{\mu}$ is greater than the elastic stressing rate. From Figure 5B, the elastic stressing rate is approximately

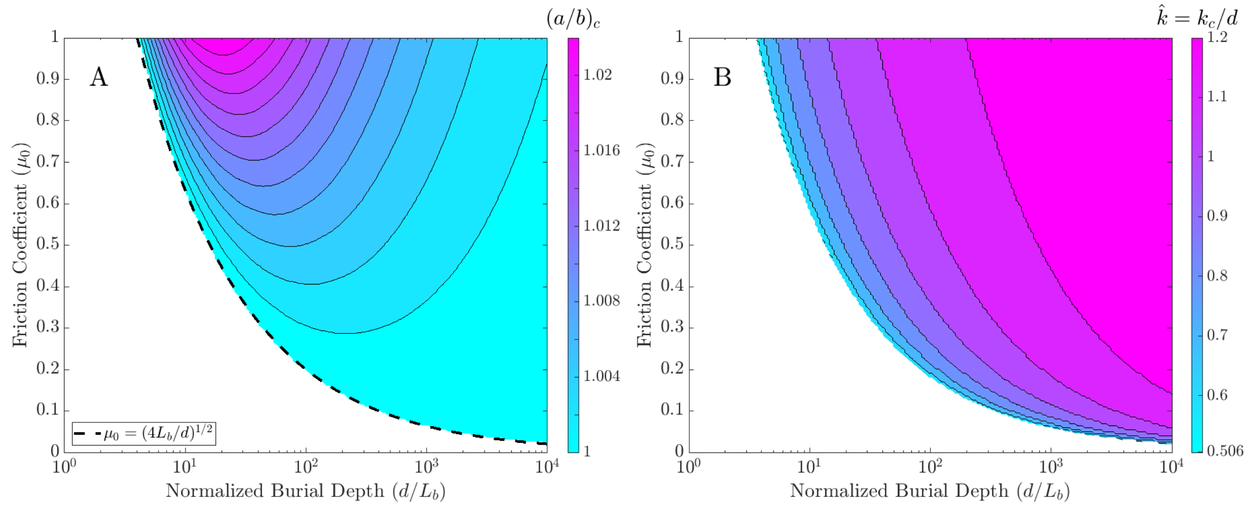

Figure 6: **(A)** Values of $(a/b)_c$, and **(B)** k_c/d for unstable behavior on infinitely long faults near a traction-free surface, as a function of friction coefficient μ_0 and normalized burial depth d/L_b. The black, dashed line in **(A)** corresponds to the shallow stability boundary given by $d = (2/\mu_0)^2 L_b$.

proportional to β/L for dip angles less than about 10° – 20°. Then for a given set of frictional parameters, when the dip angle is small only shorter length faults can relieve elastic stress faster than the frictional weakening rate. This leads to the results displayed in Figure 4.

4.3.2 Velocity-Strengthening Behavior

As noted in the Introduction, it is possible for unstable behavior to occur on velocity-strengthening faults when a coupling between slip and normal stress exists, i.e. when $N(\xi, v) \neq 0$. The parameter space for the dipping fault geometry is quite large; the stability behavior can be expected to depend on frictional and elastic parameters μ_0, a/b, L_b; burial depth d; dip angle β; and fault length L. Additionally, while normalization by h_F^* accounts for dependence on RSF and elastic parameters for velocity-weakening behavior, h_F^* does not exist on velocity-strengthening faults. Therefore the results in this section are restricted to an infinitely long fault that is parallel to a traction-free surface, which reduces the parameter space to μ_0, a/b, and a normalized burial depth d/L_b. In this case, equation (7) can be used to determine the stability of the system (see Appendix B.4 for stress change functions and details)

Figure 6 shows the results of choosing values of μ_0 and d/L_b, then determining the maximum value of $(a/b)_c = (a/b) > 1$ that satisfies $\mathrm{Re}(p) > 0$. One striking feature of the results is that unstable behavior only exists at depths greater than some minimum value that is very well approximated by $d = (2/\mu_0)^2 L_b$ (see Appendix B.4 for details). At shallower depths there are no unstable solutions to equation (7) for $(a/b) > 1$. This shallow, stable region is not related to the thin layer limit that occurs at $d/L_b \ll 1$. Where unstable behavior occurs, for constant μ_0 there is depth at which $(a/b)_c$ reaches a maximum value. While for constant d/L_b, values of $(a/b)_c$ increase monotonically with μ_0, so the velocity-strengthening instability is enhanced when friction is higher.

An extensive parameter study to determine the effects of finite fault length and dip angle is beyond the scope of this study. However, some insight can by gained be examining the critical wavelengths that correspond to the values of $(a/b)_c$. Each value of $(a/b)_c$ shown in Figure 6A occurs at some critical wavenumber k_c that is in the neighborhood of $k_c/d \approx 1$ regardless of the value of $(a/b)_c$ (Figure 6B). By analogy with the velocity weakening results, if $L^* \approx h^*/e = 2\pi/(ek_c)$, then for any set of values $[\mu_0, (a/b)_c, d/L_b]$ taken from Figure 6A, the fault length would have to be $L \geq 2\pi d/e$ for unstable behavior to occur.

5 Discussion

5.1 Some Theoretical Considerations

A main result in this paper is that linear sliding stability fundamentally depends on overall fault length. The critical fault length L^* replaces the concept of the "critical nucleation length" represented by h^*. Velocity-weakening faults are unstable if they are longer than L^*. In terms of linear behavior (where deviations from steady sliding are small), there is no minimum perturbation length scale that is needed to trigger an unstable sliding event if the fault length is longer than L^*. Velocity-weakening faults that are shorter than L^* should be considered conditionally stable, in that large perturbations out of the linear regime could generate unstable sliding events. For vertical strike-slip faults $L^* = h^*_F/e$ (Section 4.2), while for dip-slip faults the critical fault length is a function of the dip angle and burial depth (Section 4.3). For sliding systems that can be treated as a thin layer, such as landslides, glaciers, or ice streams, $L^* = h^*_L/2$.

After nucleating, the details of how an instability develops (and any related length scales) depend on the full nonlinear governing equations (*Rubin and Ampuero*, 2005, 2009; *Ampuero and Rubin*, 2008; *Viesca*, 2016a,b; *Ray and Viesca*, 2017; *Viesca*, 2023). On faults that obey the aging law, as velocities increase towards inertially limited values, sliding localizes to patches with lengths that scale with L_b (e.g. *Rubin and Ampuero*, 2005; *Viesca*, 2016a). While for the slip law, *Viesca* (2023) showed that accelerating slip localizes towards a point, so that there is no minimum patch length. Together with the results in this paper, the implication is that there is no nucleation length scale on faults that obey the slip law. This could be important, considering that recent work has shown that the slip law can explain a wider range of experimental observations than the aging law (*Bhattacharya et al.*, 2015, 2017, 2022).

However, all of the results in this paper rely on idealized fault systems that do not include complex boundary conditions or external loading; multiple interacting faults; heterogeneous frictional and material properties; or inelastic deformation. It is possible that examining more realistic finite-length fault systems may lead to different conclusions regarding nucleation length scales. In addition, the results also represent the idealizations that are incorporated into the RSF equations as they are applied to laboratory experiments. The RSF equations, including the multiple different state evolution laws, have all been determined through application of spring-slider models to experimental data (*Dieterich*, 1979; *Ruina*, 1983). Thus the possible effects of traction-free surfaces (which are numerous in most experimental geometries) on laboratory frictional behavior is mostly unknown (*Aldam et al.*, 2016).

Finally, it is clear that when examining heterogeneous systems, the fault system must be treated as a single entity. For example, applying the critical nucleation length from equation (3) to the velocity-weakening sections of a dipping fault that also has velocity-strengthening sections will result in inaccurate assessments of sliding stability. The stability behavior will instead depend on the geometrical aspects as well as the frictional properties in both the velocity-weakening and -strengthening portions of the fault (*Skarbek et al.*, 2012; *Dublanchet et al.*, 2013; *Ray and Viesca*, 2017; *Yabe and Ide*, 2017; *Luo and Ampuero*, 2018).

5.2 Some Practical Considerations

Proximity to a traction-free surface, as measured by h_F^* or L_b, has a significant influence on stability properties. Since both h_F^* and L_b are inversely proportional to effective normal stress, the normalized burial depths in Figures 4 and 6 are smaller on faults with high pore fluid pressure. This means that the influence of the free surface is enhanced on overpressured fault systems. High pore pressure leads to smaller normalized critical fault lengths, but larger values of h_F^*. If the burial depth is less than h_F^*, then the free surface will influence the stability behavior. This effect should for example be important in the shallow regions of subduction zones and in areas of induced seismicity where pore pressures can be elevated. Particularly on subduction megathrust plate boundaries, the combination of shallow dip angles and high pore pressures should lead to very small normalized critical fault lengths.

The effect of shallow burial depth on unstable behavior for velocity-strengthening faults is more complicated. For a nonzero burial depth d, a parallel fault should be the most unstable geometry, since on a dipping fault the depth from the traction-free surface will increase with down-dip distance. The values of $(a/b)_c$ for the infinite fault system in Figure 6A are close to velocity-neutral; so it seems reasonable to assume that the values would be even closer on finite-length, dipping faults that are buried. However, the velocity-weakening results show that intersecting the free surface causes a significant reduction in stability; L_D^*/h_F^* decreases logarithmically with decreasing d/h_F^*. So it is possible that values of $(a/b)_c$ may be larger on dipping faults where $d = 0$. Certainly more work is needed to understand this behavior.

Three separate effects have been established that can cause unstable sliding on velocity-strengthening faults: contrasting elastic parameters across a fault (*Rice et al.*, 2001); poroelasticity (*Heimisson et al.*, 2019); and proximity to a traction-free surface (*Aldam et al.*, 2016). All of these features are commonplace in fault systems as well as in other frictional systems like landslides and ice streams. For example, all of these effects are present in the shallow regions of subduction zones and may contribute towards enabling shallow slow slip events (e.g. *Saffer and Wallace*, 2015), or influence the behavior of tsunami earthquakes (e.g. *Bilek and Lay*, 2002).

6 Conclusion

The results in this paper show how even simple types of geometrical complexity can drastically change stability behavior. Using numerical methods makes it possible to conduct linear stability analyses for a wide range of fault systems that cannot be examined using analytical techniques. Some examples of systems for which stress change functions are available in the literature are multi-fault systems and non-planer faults in a 3D homogeneous elastic half-space (*Okada*, 1992; *Meade*, 2007). Functions are also available for different types of viscoelastic geometries (*Segall*, 2010; *Lambert and Barbot*, 2016, e.g.). Heterogeneous on-fault frictional properties can be used with any existing stress change functions (e.g. *Ray and Viesca*, 2017). Finally, numerical stability methods could also be extended to include dilatancy and changes in pore pressure, or other types of frictional constitutive behavior (e.g. *Segall and Rice*, 1995; *Chen and Spiers*, 2016; *Barbot*, 2022).

Data Availability

All of the calculations and figures in this paper can be reproduced using a MATLAB package *RSFaultZ* available at `https://github.com/rmskarbek/RSFaultZ` (*Skarbek*, 2024). The m-files for automatically generating figures are stored in the github repository directory: RSFaultZ/examples/stability.

Acknowledgments

This work was supported by the National Science Foundation under Grant No. EAR-2245540. The author thanks D. Saffer, H. Savage, and R. Viesca for discussions that helped and influenced this paper.

Appendix A Linearization of RSF Equations

Additional mathematical details are provided here for obtaining the Jacobian matrix given by equation (6). First, using equations (2) and (4), the linearized equations can be written as

$$\dot{v} = \left(\frac{\partial F_0}{\partial v}\right) v + \left(\frac{\partial F_0}{\partial \theta}\right) \theta = \left(\frac{v_0}{a}\right) \left[\frac{1}{\sigma_0}\left(\frac{\partial \dot{\tau}_E}{\partial v} - \mu_0 \frac{\partial \dot{\sigma}_E}{\partial v}\right) + \frac{b}{d_c}\right] v + \left(\frac{b v_0^3}{a d_c^2}\right) \theta \ , \tag{A1}$$

and

$$\dot{\theta} = \left(\frac{\partial H_0}{\partial v}\right) v + \left(\frac{\partial H_0}{\partial \theta}\right) \theta = -\left(\frac{1}{v_0}\right) v - \left(\frac{v_0}{d_c}\right) \theta \ . \tag{A2}$$

Equations (A1) and (A2) can be used to define a dimensional Jacobian. The elements of equation (6) are obtained after changing to the dimensionless variables defined by $\hat{t} = (v_0/d_c)t$, $\hat{v} = v/v_o$, and $\hat{\theta} = (v_0/d_c)\theta$. Dimensionless stress change functions are obtained by normalizing stresses by σ_0. So for example, $\dot{\tau}_E = T(\xi, v) = (\sigma_0 v_0/d_c)\hat{T}$.

Appendix B Stability of Spring-Slider and Infinite Fault Systems

B.1 Spring-Slider

The shear stress change in the basic spring-slider model is

$$\dot{\tau}_E = K(v_0 - v) \ , \tag{B1}$$

where K is a normalized spring stiffness with units of [Stress / Length]. Using the same dimensionless variables defined in A, the dimensionless shear stress change function is

$$\hat{T}(\hat{v}) = \frac{d_c K}{\sigma_0}(1 - \hat{v}) \ . \tag{B2}$$

Inserting the derivative of equation (B2) with respect to $\hat{v}$ into equation (8) and setting the left-hand side equal to zero yields the critical stiffness $K_c = \sigma_0(b - a)/d_c$.

B.2 Full-Space

For infinite faults the critical wavelength can be found by searching for solutions of the form $v(\xi, t) = A \exp(pt + ik\xi)$. For a full-space, the shear stress change function can be found by substituting this expression into equation (16), for $L \to \infty$; this is essentially the method used by (*Rice et al.*, 2001):

$$T(\xi, v) = ikA \left(\frac{G'}{2\pi}\right) \int_{-\infty}^{\infty} \frac{\exp(pt + iks)}{s - \xi} ds \ . \tag{B3}$$

After making a change of variables $u = s - \xi$, equation (B3) becomes

$$\begin{aligned} T(\xi, v) &= ik\left(\frac{G'}{2\pi}\right) A\exp(pt + ik\xi) \int_{-\infty}^{\infty} \frac{\exp(iku)}{u} du \\ &= -\left(\frac{|k|G'}{2}\right) v \ , \end{aligned} \tag{B4}$$

where the integral in the first line is a Fourier Transform of $1/u$ and is equal to $i\pi\mathrm{sgn}(k)$. Using the previously defined dimensionless variables, but leaving k in dimensional form, the critical wavenumber k_c from equation (8) is

$$\left(\frac{b}{a}\right)\left(1 - \frac{L_b|k_c|}{2}\right) - 1 = 0 \ , \tag{B5}$$

which leads to equation (3) since the critical wavelength is defined as $h_F^* = \lambda_c = 2\pi/k_c$.

B.3 Thin Layer

The critical wavelength for the thin layer system can be found by following the same procedure for the full-space system, but using equation (11) for the shear stress change function.

$$T(\xi, v) = (dE')\frac{\partial^2}{\partial\xi^2}[A\exp(pt + ik\xi)] = -dE'k^2 v \ . \tag{B6}$$

Using the dimensionless variables as before, equation (8) becomes

$$\left(\frac{b}{a}\right)\left[1 - (L_{bh}k_c)^2\right] - 1 = 0 \ , \tag{B7}$$

with $L_{bh} = \sqrt{dE'd_c/(b\sigma_0)}$ (*Viesca*, 2016b). Solving equation (B7) for the critical wavelength leads to equation (12) for h_L^*.

B.4 Velocity-Strengthening Layer

The stress change functions for in-plane sliding on an infinitely long fault that is parallel to a traction-free surface at a depth d are (e.g. *Viesca*, 2016a)

$$\begin{aligned} T(\xi, v) = \frac{G}{2\pi(1-\nu)} \int_{-\infty}^{\infty} \Bigg\{ & \frac{1}{s-\xi} - \frac{s-\xi}{4d^2 + (s-\xi)^2} + \frac{8d^2(s-\xi)}{[4d^2 + (s-\xi)^2]^2} \\ & + \frac{4d^2(s-\xi)^3 - 48d^4(s-\xi)}{[4d^2 + (s-\xi)^2]^3} \Bigg\} \frac{\partial v}{\partial s} ds \ , \end{aligned} \tag{B8}$$

and

$$N(\xi, v) = \frac{G}{2\pi(1-\nu)} \int_{-\infty}^{\infty} \left\{ \frac{32d^5 - 24d^3(s-\xi)^2}{[4d^2 + (s-\xi)^2]^3} \right\} \frac{\partial v}{\partial s} ds \ . \tag{B9}$$

The stability of this system is most easily determined after applying a Fourier transform. Using the Fourier transform pair:

$$\tilde{f}(k) = F[f(x)] = \int_{-\infty}^{\infty} f(x) e^{-ikx} dx \tag{B10}$$

$$f(x) = F^{-1}[\tilde{f}(k)] = \frac{1}{2\pi} \int_{-\infty}^{\infty} \tilde{f}(k) e^{ikx} dx \ , \tag{B11}$$

equations (B8) and (B9) become

$$\widetilde{T}(k,\tilde{v}) = -\left(\frac{G'|k|}{2}\right)\left\{1 - e^{-2d|k|}\left[1 - 2d|k| + 2(dk)^2\right]\right\}\tilde{v}\ , \tag{B12}$$

and

$$\widetilde{N}(k,\tilde{v}) = -iG'k(dk)^2 e^{-2d|k|}\tilde{v}\ . \tag{B13}$$

where tildes denote transformed quantities. Note that these functions are provided by (*Viesca*, 2016a) using a different transform pair.

The eigenvalues p can then be computed from equation (7) after defining $\Gamma = (1/b)(\widetilde{T}_{\tilde{v}} - \mu_0\widetilde{N}_{\tilde{v}})$ using equations (B12) and (B13). Using the dimensionless variables, and also defining $\hat{k} = dk$ yields

$$\Gamma = -\left(\frac{L_b}{d}\right)\left\{\frac{|\hat{k}|}{2}\left[1 - e^{-2|\hat{k}|}\left(1 - 2|\hat{k}| + 2\hat{k}^2\right)\right] - i\mu_0\hat{k}^3 e^{-2\hat{k}}\right\}\ . \tag{B14}$$

The resulting equation for p is complex and depends on the values of (a/b), (L_b/d), μ_0, and the dimensionless wavenumber $\hat{k}$. The results in Figure 6 were obtained through an iterative process by solving for p numerically as a function of $\hat{k}$ for chosen values of L_b/d and μ_0. For each pair of values $(L_b/d, \mu_0)$, $p(\hat{k})$ was first determined for a value of $(a/b) < 1$, which guarantees that $\mathrm{Re}[p(\hat{k})] > 0$ for some value of $\hat{k}$; numerical tests showed that the maximum value of $p(\hat{k})$ occurs in the vicinity of $\hat{k} \approx 1$. This process was then repeated for incrementally larger values of (a/b) until $\mathrm{Re}[p(\hat{k})] < 0$ for all values of $\hat{k}$, which determines the values of $(a/b)_c$ shown in Figure 6A.

The minimum depth for unstable behavior can be approximately determined by solving for p for a specific value of $\hat{k}$. From the results in Figure 6B, the stability boundary occurs at $\hat{k} \approx 0.5$, so that

$$\Gamma = -\left(\frac{L_b}{d}\right)\left[\left(\frac{2 - e^{-1}}{8}\right) - i\mu_0\left(\frac{e^{-1}}{8}\right)\right]\ . \tag{B15}$$

Additionally, that stability boundary occurs at $(a/b) = 1$. With these values of $\hat{k}$ and (a/b), equation (7) becomes

$$p^2 - \left(\frac{L_b}{d}\right)\left[\left(\frac{2 - e^{-1}}{8}\right) - i\mu_0\left(\frac{e^{-1}}{8}\right)\right]p + \left(\frac{L_b}{d}\right)\left[\left(\frac{2 - e^{-1}}{8}\right) - i\mu_0\left(\frac{e^{-1}}{8}\right)\right] = 0\ . \tag{B16}$$

Now p can be solved for using a procedure described in *Rice et al.* (2001). First, Figure 6 indicates that for a constant value of μ_0, the real part of p changes sign as d/L_b increases from zero. The sign change occurs at $p = i\rho$; substituting this into equation (B16) yields

$$\left[-\rho^2 - \left(\frac{\mu_0 e^{-1}L_b}{8d}\right)\rho + \frac{(2 - e^{-1})L_b}{8d}\right] - i\left(\frac{L_b}{d}\right)\left[\left(\frac{2 - e^{-1}}{8}\right)\rho + \frac{\mu_0 e^{-1}}{8}\right] = 0\ . \tag{B17}$$

Equation (B17) is satisfied when both its real and imaginary parts are equal to zero. Setting the real part equal to zero provides an equation for ρ in terms of μ_0 and (L_b/d):

$$\rho = -\left(\frac{\mu_0 e^{-1}L_b}{16d}\right) \pm \frac{1}{2}\sqrt{\left(\frac{\mu_0 e^{-1}L_b}{8d}\right)^2 - \frac{(2 - e^{-1})L_b}{2d}}\ . \tag{B18}$$

Finally, inserting equation (B18) into the imaginary part of equation (B17) and setting it equal to zero provides an equation for d/L_b as a function of μ_0. The best way to execute this final step is using a symbolic math program. The solution is

$$\frac{d}{L_b} = \frac{1}{8e}\left[\frac{(2e-1)(1-2e)^2}{\mu_0^2} - 1\right] + 1/4 \approx \left(\frac{2}{\mu_0}\right)^2\ . \tag{B19}$$

Appendix C Dip-slip Faults

Consider an edge dislocation in a 2D homogeneous elastic body. The dislocation induces displacement and stress fields throughout the elastic body that can be represented in terms of two complex potentials, $\omega(z)$ and $\Omega(z)$, that are analytic functions of z (e.g. *England*, 2003; *Bower*, 2009). The complex coordinate z is defined as $z = x + iy = re^{i\phi}$ where (r, ϕ) are radial coordinates with ϕ measured from the x-axis in the direction of the y-axis.

For the dipping fault system shown in Figure 1C, the fault is located at $\beta_0 = \pi - \beta$ along $l \leq r \leq l + L$, where $l = d/\sin(\beta)$, (also note that $\xi = r$). The stress change functions can be obtained by considering a distribution of dislocations along the fault, and computing the shear and normal stresses that these dislocations induce on the fault itself. The first and most important step is to determine the complex potentials for a single dislocation placed at $z_0 = r_0 e^{i\beta_0}$, with Burger's vector $be^{i\beta_0} = b\cos(\beta_0) + ib\sin(\beta_0)$ (e.g. *Freund and Barnett*, 1976).

In the x-y plane the stress and displacement fields are given by:

$$\sigma_x + \sigma_y = 2\left[\Omega'(z) + \overline{\Omega'(z)}\right] , \tag{C1}$$

$$\sigma_y - i\sigma_{xy} = \Omega'(z) + \overline{\Omega'(z)} + z\overline{\Omega''(z)} + \omega'(z) , \tag{C2}$$

$$2G(u_x + iu_y) = (3 - 4\nu)\Omega(z) - z\overline{\Omega'(z)} - \overline{\omega(z)} , \tag{C3}$$

where primes denote derivatives with respect to z, and bars denote complex conjugates (e.g. *England*, 2003, Section 2.5). The displacements are denoted by u_x, u_y; the normal stresses by σ_x and σ_y, and σ_{xy} is the shear stress. The normal and shear stresses on the fault can be obtained in the radial coordinate system, in which case the stresses are

$$\sigma_r + \sigma_\phi = 2\left[\Omega'(z) + \overline{\Omega'(z)}\right] , \tag{C4}$$

$$\sigma_\phi - i\sigma_{r\phi} = \Omega'(z) + \overline{\Omega'(z)} + e^{-2i\phi}[z\overline{\Omega''(z)} + \omega'(z)] , \tag{C5}$$

$$2G(u_r + iu_\phi) = e^{-2i\phi}[(3 - 4\nu)\Omega(z) - z\overline{\Omega'(z)} - \overline{\omega(z)}] . \tag{C6}$$

For a half-space with a traction-free surface at $y = 0$, $z = x$, the potentials can be written as

$$\Omega(z) = \Omega_0(z) + \Omega_1(z) , \qquad \omega(z) = \omega_0(z) + \omega_1(z) , \tag{C7}$$

where $\Omega_0(z)$ and $\omega_0(z)$ are the potentials for a full-space, and so will produce tractions along $z = x$; while $\Omega_1(z)$ and $\omega_1(z)$ are additional potentials that clear the tractions along $z = x$. The full-space potentials are given by (e.g. *Bower*, 2009, Section 5.3.12)

$$\Omega_0(z) = \gamma \ln(z - z_0) , \tag{C8}$$

$$\omega_0(z) = \overline{\gamma} \ln(z - z_0) - \frac{\gamma \overline{z}_0}{z - z_0} , \tag{C9}$$

where

$$\gamma = -\frac{iGbe^{i\beta_0}}{4\pi(1 - \nu)} . \tag{C10}$$

The additional potentials can be found using a variety of methods (e.g. *Dmowska and Kostrov*, 1973; *Freund and Barnett*, 1976). Here, the additional potentials are computed using the process of analytic continuation (e.g. *England*, 2003, Section 3.5), and are given by

$$\Omega_1(z) = -z\overline{\Omega_0'(\overline{z})} - \overline{\omega_0(\overline{z})} , \tag{C11}$$

$$\omega_1(z) = z\overline{\omega_0'(\overline{z})} - \overline{\Omega_0(\overline{z})} + z\overline{\Omega_0'(\overline{z})} + z^2\overline{\Omega_0''(\overline{z})} . \tag{C12}$$

Substituting these definitions for $\Omega_1(z)$ and $\omega_1(z)$ into equations (C7) along with the results for $\Omega_0(z)$ and $\omega_0(z)$, the potentials for an edge dislocation in a half-space are:

$$\Omega(z) = \gamma \ln\left[\frac{z - z_0}{z - \overline{z}_0}\right] - \frac{\overline{\gamma}(z - z_0)}{z - \overline{z}_0} \ , \tag{C13}$$

$$\omega(z) = \overline{\gamma} \ln\left[\frac{z - z_0}{z - \overline{z}_0}\right] - \frac{\gamma \overline{z}_0}{z - z_0} + \frac{\gamma z}{z - \overline{z}_0} + \frac{\overline{\gamma}(z_0 - \overline{z}_0)z}{(z - \overline{z}_0)^2} \ . \tag{C14}$$

Note that equations (A4) and (A5) in *Rudnicki and Wu* (1995) are the derivatives of equations (C13) and (C14).

The normal σ_ϕ and shear $\sigma_{r\phi}$ stresses on the fault due to a single dislocation are given by the real and imaginary parts of equation (C5), evaluated using equations (C13) and (C14) at values of z corresponding to $\phi = \beta_0$ and $l \leq \xi \leq l + L$. For a distribution of dislocations along the length of the fault, the resultant Burger's vector between neighboring points ξ and $\xi + d\xi$ is $b = (\partial\delta/\partial\xi)d\xi$, where $\delta(\xi)$ is slip on the fault (*Weertman*, 1996; *Freund and Barnett*, 1976). The stress change functions are found by integrating over the length of the fault, such that

$$T(\xi, \delta) = -\int_l^{l+L} \mathrm{Im}\left\{\Omega'(z) + \overline{\Omega'(z)} + e^{-2i\beta_0}[z\overline{\Omega''(z)} + \omega'(z)]\right\} \frac{\partial \delta}{\partial s} ds \ , \tag{C15}$$

$$N(\xi, \delta) = \int_l^{l+L} \mathrm{Re}\left\{\Omega'(z) + \overline{\Omega'(z)} + e^{-2i\beta_0}[z\overline{\Omega''(z)} + \omega'(z)]\right\} \frac{\partial \delta}{\partial s} ds \ , \tag{C16}$$

where the potentials are evaluated using equations (C13) and (C14) at $z = \xi e^{i\beta_0}$ and $z_0 = s e^{i\beta_0}$. Finally, note that it is possible to write the integrands in equations (C15) and (C16) explicitly in terms of ξ and β_0, however the resulting expressions are extremely cumbersome [see for example equations (13) in *Freund and Barnett* (1976); equations (3.1) – (3.2) in *Dmowska and Kostrov* (1973); or equations (A6) – (A11L) in *Rudnicki and Wu* (1995)]. For numerical computations it is most concise to compute the stresses using the individual equations listed above.

References

Aldam, M., Y. Bar-Sinai, I. Svetlizky, E. A. Brener, J. Fineberg, and E. Bouchbinder (2016), Frictional sliding without geometrical reflection symmetry, *Phys. Rev. X*, *6*, 041,023, doi:10.1103/PhysRevX.6.041023.

Ampuero, J.-P., and A. M. Rubin (2008), Earthquake nucleation on rate and state faults - Aging and slip laws, *J. Geophys. Res.*, *113*, B01302, doi:10.1029/2007JB005082.

Barbot, S. (2022), A rate-, state-, and temperature-dependent friction law with competing healing mechanisms, *J. Geophys. Res.*, *127*(11), e2022JB025,106, doi:https://doi.org/10.1029/2022JB025106.

Bhattacharya, P., A. M. Rubin, E. Bayart, H. M. Savage, and C. Marone (2015), Critical evaluation of state evolution laws in rate and state friction: Fitting large velocity steps in simulated fault gouge with time-, slip-, and stress-dependent constitutive laws, *J. Geophys. Res.*, *120*(9), 6365–6385, doi:10.1002/2015JB012437.

Bhattacharya, P., A. M. Rubin, and N. M. Beeler (2017), Does fault strengthening in laboratory rock friction experiments really depend primarily upon time and not slip?, *J. Geophys. Res.*, *122*(8), 6389–6430, doi:10.1002/2017JB013936.

Bhattacharya, P., A. M. Rubin, T. E. Tullis, N. M. Beeler, and K. Okazaki (2022), The evolution of rock friction is more sensitive to slip than elapsed time, even at near-zero slip rates, *Proc. Natl. Acad. Sci. U. S. A.*, *119*(30), e2119462,119, doi:10.1073/pnas.2119462119.

Bilek, S. L., and T. Lay (2002), Tsunami earthquakes possibly widespread manifestations of frictional conditional stability, *Geophys. Res. Lett.*, *29*(14), 18–1–18–4, doi:10.1029/2002GL015215.

Bower, A. F. (2009), *Applied mechanics of solids*, CRC press.

Chen, J., and C. J. Spiers (2016), Rate and state frictional and healing behavior of carbonate fault gouge explained using microphysical model, *J. Geophy. Res.*, *121*(12), 8642–8665, doi:https://doi.org/10.1002/2016JB013470.

Dieterich, J. H. (1979), Modeling of rock friction: 1. Experimental results and constitutive equations, *J. Geophys. Res.*, *84*(B5), 2161–2168, doi:10.1029/JB084iB05p02161.

Dieterich, J. H. (1992), Earthquake nucleation on faults with rate- and state-dependent strength, *Tectonophysics*, *211*(1-4), 115–134, doi:10.1016/0040-1951(92)90055-B.

Dmowska, R., and B. V. Kostrov (1973), A shear crack in a semi-space under plane strain conditions, *Archives of Mechanics*, *25*(3), 421 – 440.

Dublanchet, P., P. Bernard, and P. Favreau (2013), Interactions and triggering in a 3-d rate-and-state asperity model, *J. Geophys. Res.*, *118*(5), 2225–2245, doi:https://doi.org/10.1002/jgrb.50187.

England, A. H. (2003), *Complex variable methods in elasticity*, Courier Corporation.

Freund, L. B., and D. M. Barnett (1976), A two-dimensional analysis of surface deformation due to dip-slip faulting, *Bull. Seismol. Soc. Am.*, *66*(3), 667, errata, Bull. Seismol. Soc. Am., 66, 2083-2084, 1976.

Heimisson, E. R., E. M. Dunham, and M. Almquist (2019), Poroelastic effects destabilize mildly rate-strengthening friction to generate stable slow slip pulses, *J. Mech. Phys. Solids*, *130*, 262 – 279, doi:https://doi.org/10.1016/j.jmps.2019.06.007.

Horowitz, F. G., and A. Ruina (1989), Slip patterns in a spatially homogeneous fault model, *J. Geophys. Res.*, *94*(B8), 10,279–10,298, doi:https://doi.org/10.1029/JB094iB08p10279.

Kato, N., and T. Hirasawa (1997), A numerical study on seismic coupling along subduction zones using a laboratory-derived friction law, *Phys. Earth Planet. Inter.*, *102*(1), 51–68, doi:https://doi.org/10.1016/S0031-9201(96)03264-5.

Lambert, V., and S. Barbot (2016), Contribution of viscoelastic flow in earthquake cycles within the lithosphere-asthenosphere system, *Geophys. Res. Lett.*, *43*(19), 10,142–10,154, doi:https://doi.org/10.1002/2016GL070345.

Liu, Y., and J. R. Rice (2007), Spontaneous and triggered aseismic deformation transients in a subduction fault model, *J. Geophys. Res.*, *112*, B09404, doi:10.1029/2007jb004930.

Luís, R. (2021), Linear stability conditions for a first order n-dimensional mapping, *Qualitative theory of dynamical systems*, *20*(1), 20, doi:https://doi.org/10.1007/s12346-021-00455-z.

Luo, Y., and J.-P. Ampuero (2018), Stability of faults with heterogeneous friction properties and effective normal stress, *Tectonophysics*, *733*, 257–272, doi:https://doi.org/10.1016/j.tecto.2017.11.006.

Marone, C. (1998), Laboratory-derived friction laws and their application to seismic faulting, *Annu. Rev. Earth Planet. Sci.*, *26*, 643–696, doi:10.1146/annurev.earth.26.1.643.

Meade, B. J. (2007), Algorithms for the calculation of exact displacements, strains, and stresses for triangular dislocation elements in a uniform elastic half space, *Computers & Geosciences*, *33*(8), 1064–1075, doi:https://doi.org/10.1016/j.cageo.2006.12.003.

Okada, Y. (1992), Internal deformation due to shear and tensile faults in a half-space, *Bull. Seismol. Soc. Am.*, *82*(2), 1018.

Pivato, M. (2010), *Linear Partial Differential Equations and Fourier Theory*, Cambridge University Press, doi:10.1017/CBO9780511810183.

Ray, S., and R. C. Viesca (2017), Earthquake nucleation on faults with heterogeneous frictional properties, normal stress, *J. Geophys. Res.*, *122*(10), 8214–8240, doi:10.1002/2017JB014521.

Rice, J., and A. L. Ruina (1983), Stability of steady frictional slipping, *Journal of applied mechanics*, *50*(2), 343–349, doi:10.1115/1.3167042.

Rice, J. R., N. Lapusta, and K. Ranjith (2001), Rate and state dependent friction and the stability of sliding between elastically deformable solids, *Journal of the Mechanics and Physics of Solids*, *49*(9), 1865 – 1898, doi:http://dx.doi.org/10.1016/S0022-5096(01)00042-4.

Rubin, A. M., and J.-P. Ampuero (2005), Earthquake nucleation on (ageing) rate and state faults, *J. Geophys. Res.*, *110*, B11312, doi:10.1029/2005JB003686.

Rubin, A. M., and J.-P. Ampuero (2009), Self-similar slip pulses during rate-and-state earthquake nucleation, *J. Geophys. Res.*, *114*(B11), doi:https://doi.org/10.1029/2009jb006529.

Rudnicki, J. W., and M. Wu (1995), Mechanics of dip-slip faulting in an elastic half-space, *J. Geophys. Res.*, *100*(B11), 22,173–22,186, doi:https://doi.org/10.1029/95JB02246.

Ruina, A. (1983), Slip instability and state variable friction laws, *J. Geophys. Res.*, *88*, 10,359–10,370.

Saffer, D. M., and L. M. Wallace (2015), The frictional, hydrologic, metamorphic and thermal habitat of shallow slow earthquakes, *Nat. Geosc.*, *8*, 594 – 600, doi:10.1038/ngeo2490.

Scholz, C. H. (2019), *The Mechanics of Earthquakes and Faulting*, Cambridge University Press, Singapore.

Segall, P. (2010), *Earthquake and Volcano Deformation*, 424 pp., Princeton Univ. Press, Princeton, N.J.

Segall, P., and J. R. Rice (1995), Dilatancy, compaction, and slip instability of a fluid infiltrated fault, *J. Geophys. Res.*, *100*, 22,155–22,171.

Skarbek, R. M. (2024), rmskarbek/RSFaultZ: v1.0, doi:10.5281/zenodo.10497312.

Skarbek, R. M., A. W. Rempel, and D. A. Schmidt (2012), Geologic heterogeneity can produce aseismic slip transients, *Geophys. Res. Lett.*, *39*(21), doi:10.1029/2012GL053762.

Strogatz, S. H. (2018), *Nonlinear dynamics and chaos with student solutions manual: With applications to physics, biology, chemistry, and engineering*, CRC press, doi:https://doi.org/10.1201/9780429492563.

Viesca, R. C. (2016a), Stable and unstable development of an interfacial sliding instability, *Phys. Rev. E*, *93*, 060,202, doi:10.1103/PhysRevE.93.060202.

Viesca, R. C. (2016b), Self-similar slip instability on interfaces with rate- and state-dependent friction, *Proc. R. Soc. A*, *472*(2192), doi:10.1098/rspa.2016.0254.

Viesca, R. C. (2023), Frictional state evolution laws and the non-linear nucleation of dynamic shear rupture, *J. Mech. Phys. Solids*, *173*, 105,221, doi:https://doi.org/10.1016/j.jmps.2023.105221.

Weertman, J. (1996), *Dislocation Based Fracture Mechanics*, World Scientific, doi:10.1142/3062.

Yabe, S., and S. Ide (2017), Slip-behavior transitions of a heterogeneous linear fault, *J. Geophys. Res.*, *122*(1), 387–410, doi:https://doi.org/10.1002/2016JB013132.